SAND2017-3110C

ILASS-Americas 29th Annual Conference on Liquid Atomization and Spray Systems, Atlanta, GA, May 2017

Quantitative, Bias-Corrected Measurements of Droplet Position, Size and Velocity with Digital In-line Holography

Yi Chen and Daniel R. Guildenbecher
Sandia National Laboratories
P.O. Box 5800
Albuquerque, NM 87185, USA

Abstract

Digital in-line holography (DIH) is a laser diagnostic technique that can be used to measure particle sizes, velocities and positions in sprays and other multiphase flows. Understanding the biases, error sources and limitations of DIH are critical to designing processing algorithms and making accurate quantitative measurements. Here, work focuses specifically on the biases which arise whenever there is a non-constant correlation between particle size and particle velocity. Due to the limited data throughput of digital sensors, one often has to choose between high-temporal resolution with a limited spatial resolution (image pixel count) or high-spatial resolution with limited temporal resolution. As shown here, when particle sizes are sampled in space with insufficient frame rates for particle tracking through time, the measured particle size distribution is biased toward particle sizes classes which travel slower and reside within the field-of-view longer. Such biases due to size-velocity correlations have been previously reported for many spray diagnostics and are shown here to be equally applicable to DIH. Using simulations and experiments, corrections are proposed and validated which reduce these biases using a measurement of the mean particle size to velocity correlation. Finally, it is proposed to combine a high-spatial resolution measurement with a simultaneous temporally resolved measurement. As demonstrated here, this allows for a relatively large particle size dynamic range, which is corrected for size-velocity biases.

Introduction

Accurate statistics of disperse particles in liquid sprays and other multiphase flows is essential for understanding the underlying processes and for generating precise models. In order to investigate these statistics, a wide range of optical and collection based measurement techniques have been developed. Detailed reviews of the various methods are provided by Lefebvre [1], Bachalo [2], Tropea [3], Gouesbet and Gréhan [4], and Xu [5], among many others. Each technique has specific advantages while also suffering from measurement uncertainty and biases which must be carefully considered in order to achieve accurate results.

Digital In-line Holography (DIH) is a somewhat recent addition to this suite of multiphase flow diagnostics [6]. In DIH a coherent laser beam propagates through the particle field. Resulting diffraction patterns are imaged as the hologram. Following recording, the digital hologram is numerically refocused along the optical depth via solution of the diffraction integral equation. The result is a 3D image of the original particle field. With automatic data processing routines, in-focus particle sizes and shapes are measured at their original depth [7-12]. By quantifying many particles from one or more holograms, statistics of the underlying particle field can be measured.

As an example, Figure 1(a) shows one hologram image of particles from the breakup of a water column in the convective flow behind a shockwave. Further details on the experimental configuration and results are given in subsequent sections of this paper and some other initial work [13-15]. Diffraction patterns from individual particles are clearly observed. This image can be numerically refocused throughout depth as demonstrated by Figure 1(b), which shows the refocused results at the approximate center of the particle field (optical depth, $z = 80$ mm). Finally, using the methods discussed in [7, 9, 10, 12], individual 3D particle positions, in-focus sizes, and velocities are automatically quantified as shown in Figure 1(c).

Like all measurement techniques, DIH suffers from certain measurement uncertainty and biases. Much previous work has shown that positional uncertainty is significantly higher in the optical depth direction due to the limited angular aperture from which the depth is reconstructed [16, 17]. Additional work has demonstrated that positional as well as particle size uncertainty is also a strong function of the chosen processing methodologies [12]. Finally, as is clearly demonstrated in Figure 1, DIH is further challenged when particles appear to overlap one another within the field of view. This has led Malek *et al.* [18] and others to define an apparent shadow density, above which the uncertainty from overlapping particles is too severe for practical measurements.

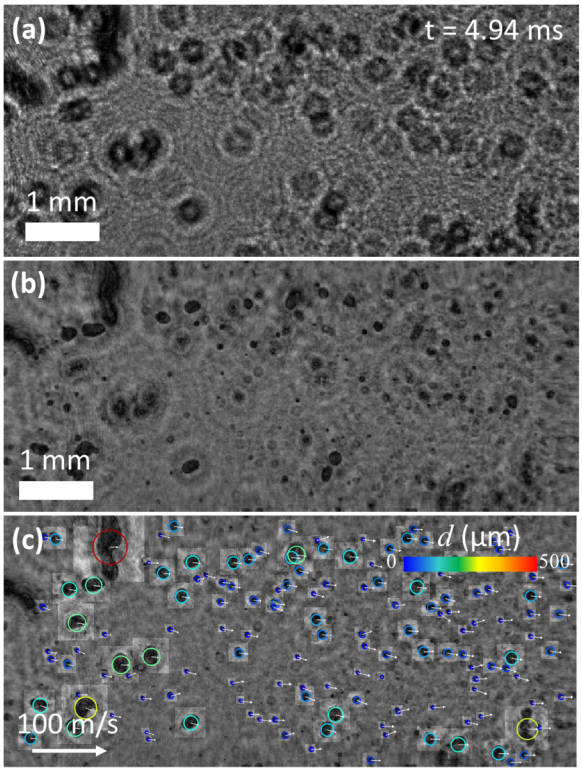

Figure 1. Example DIH results from the experiments discussed here. (a) raw hologram image from the 2× FOV, (b) numerically refocused to $z = 80$ mm, and (c) particle positions, sizes, and velocities tracked from the DIH video results. The test conditions begin with a 1 mm diameter column subjected to 30 m/s convective flow, giving a Weber number $We = 12.6$. Cameras were placed 22 mm downstream from the initial water column.

While these sources of uncertainty are certainly important and warrant further investigation, in many practical flow measurements the additional measurement biases which arise from size-velocity correlations are equally or possibly more important. However, perhaps due to the somewhat more abstract manner in which this phenomenon affects measurement accuracy, it has been the authors' experience that uncertainty in measured particle size distributions due to size-velocity correlations are the least well-understood or acknowledged in the recent literature.

As an introduction, consider the simple case illustrated in Figure 2. Here, two droplet generators are assumed to each produce one drop per second. The top droplet generator produces large drops moving at velocity v_0, while the bottom generator produces a stream of smaller drops moving at $2v_0$. Due to the difference in velocities, the larger, slower droplets are spaced at half the distance of the smaller, faster droplets. When a snapshot of this particle field is recorded at the downstream distance shown, there are twice as many large

droplets within the field-of-view compared to small droplets. Measurements such as this, which quantify particle statistics from snapshot images, are common in the literature including the authors' own use of DIH [8, 11]. However, when such techniques are used to estimate boundary conditions, perhaps for input to spray simulations, this measure of the particle field is often not the desired quantity. Rather, the rate of droplet production is more typically desired. For the current example, if the correlation between droplet size and velocity is not measured or known, then the imaging results would incorrectly imply a flow rate of big drops twice that of small drops.

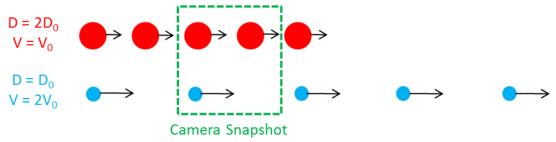

Figure 2. Conceptual illustration of the effects of size-velocity correlations. Here both generators produce drops at the same rate, yet the spatial concentration of larger droplets is higher due to their slower velocity.

In many spray applications, aerodynamic drag tends to affect droplets of different size classes at dissimilar rates. As a result, correlations between mean droplet size and velocity are common, and as discussed by Lefebvre [1] and many others, biases in particle size distributions due to size-velocity correlations have long been recognized to affect many spray measurement techniques. Here, we review the effects of size-velocity correlations on DIH measurements and discuss opportunities to extend the DIH technique for improved accuracy and size dynamic range. The work begins with a review of the simple theory for correcting size-velocity correlations, which is shown to be equally applicable to DIH results. Following this, the theory is applied to some practical experimental results and conclusions are discussed.

Before proceeding, it is noted that much of the discussion here is equally valid for any image based particle measurement techniques. With widespread availability of digital cameras, high-speed recording, and image processing techniques, image based particle sizing has become common. Whether or not holography methods are used to extend imaging to 3D, all image based methods have the potential to suffer from the size-velocity correlation biases discussed here.

Experimental configuration

The experimental results presented here are taken from the investigation of the breakup of a liquid column in a shock-induced cross-flow as discussed in [13-15]. As illustrated in Figure 3, a gas-phase shock tube is used to produce an approximately one dimensional shock-wave which propagates through the test section. Immediately before firing of the shock tube, a slow moving, laminar jet (column) of water is established within the test section. After firing, strong convective flow behind the shock-wave creates aerodynamic forces which tend to distort and eventually fragment the water column.

To capture DIH images, the 532 nm output from a continuous laser (Coherent Verdi V6) is spatially filtered and collimated before passing through the test section. Resulting diffraction patterns are recorded with two high-speed cameras (Photron SA-Z). One camera uses a ~6× magnification objective and records at the maximum pixel resolution (1024×1024 pixels) with corresponding frame rate of 20,000 fps. Unfortunately, at this relatively high magnification, individual particles traverse through the field-of-view (FOV) within a few frames (typically 3-4 frames depending on particle velocities). Given the other sources of uncertainty in DIH, particle residence times are found to be insufficient to accurately track individual particles as a function of time and record their velocity. To address this, the second camera is configured with a lower magnification objective (~2×), resulting in a larger FOV. In addition, this camera records a sub-set of the total pixels (640×260 pixels) which enables a faster record rate of 100,000 fps. With this, particle residence times are found to be sufficient for accurate tracking and velocity measurements. In summary, the experiment consists of two simultaneous DIH recordings, one with a 3.6×3.6 mm FOV at 20,000 fps with ultimate pixel resolution of 3.5 μm and a second with 8.0×3.3 mm FOV at 100,000 fps with ultimate pixel resolution of 12.5 μm.

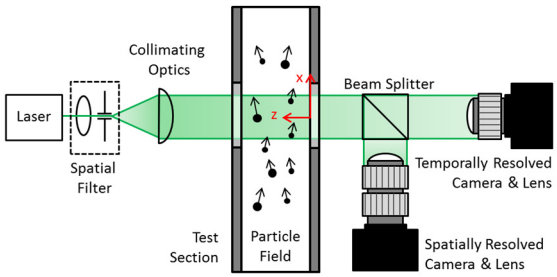

Figure 3. Experimental configuration with spatially resolved camera (6× magnification) and temporally resolved camera (2× magnification).

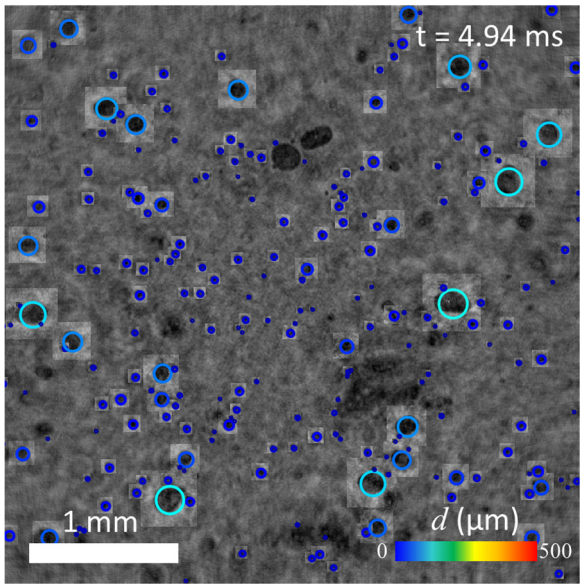

Figure 4. Example DIH results from the spatially resolved cameras (6× FOV) recorded at approximately the same instant as the 2× data in Figure 1.

Data processing to extract particle information from the DIH videos is summarized here and has been discussed in more detail elsewhere [7, 13-15]. First, all individual frames from both the 2× and 6× are processed using the methods in [9, 10, 12] to measure the 3D position and in-focus sizes and morphologies of each discrete particle. For example, Figure 4 shows the results from one frame of the 6× FOV at approximately the same instant as Figure 1. Next the 2× data is further processed using the methods in [7] to attempt to track individual particles through the FOV. If completely successful, the result is a 3D quantification of individual particle trajectories, which begin and end at the instant when the particle enters and leaves the FOV, respectively. In this manner, each individual particle is tracked once and only once and can be assigned a mean diameter and three-component velocity. (The image in Figure 1(c) shows a snapshot of the 2× results which have been processed in this manner.)

From the experimental videos, with select images summarized in Figure 1 and Figure 4, the raw measured particle size distributions are constructed as shown in Figure 5. Figure 5(a) compares the particle size probability distribution functions (PDF) by number between the 6× and 2× FOVs, while Figure 5(b) show the probability density weighted by the volume within each bin. In both cases, it is clear that the probability densities from the two FOVs do not perfectly agree. For one, the 6× FOV allows for measurement of smaller particles, and therefore contains data within a larger size dynamic range. The limited size dynamic range of the 2× DIH (or any image based measurement) is particularly stark due to the use of the high-speed cameras with a limited pixel window for fast record rates. Later in this work, some methods are proposed which combing data from the two FOVs to effectively expand the size dynamic range for accurate measurements.

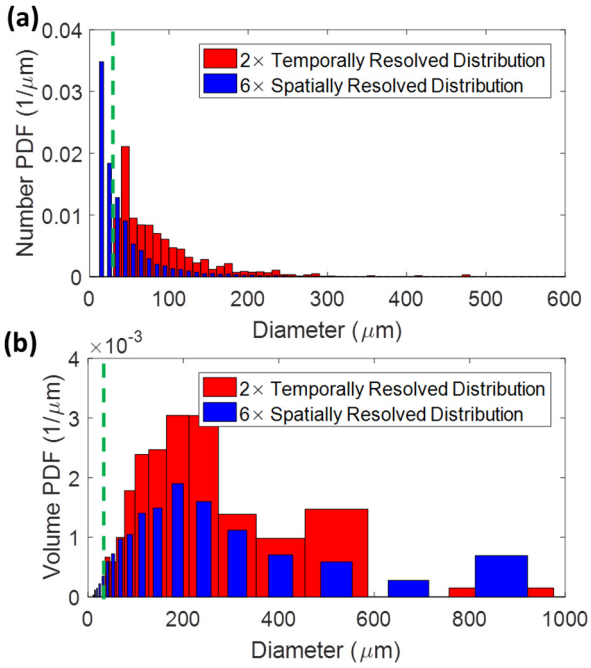

Figure 5. Comparison of the raw particle size probability densities measured from the two experimental FOVs. (a) weighted by count, and (b) weighted by volume. The experiments contained N_t = 30,598 tracked particles for the 2× FOV and N_s = 10,230 correlated (un-tracked) particles from the 6× FOV from two experimental instances at the same conditions.

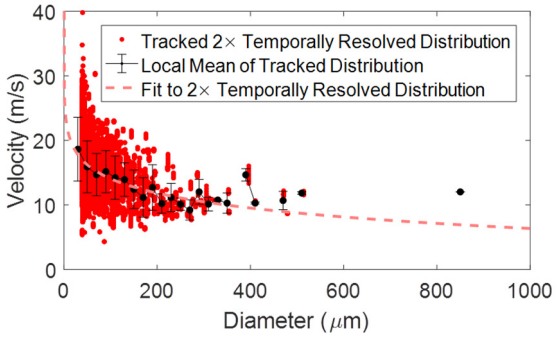

Figure 6. Size-velocity correlation measured from the 2× temporally resolved FOV.

Even more important to the current discussion, the probability densities from the two FOVs also differ

due to the effects of the size-velocity correlation. Figure 6 shows a scatter plot of the measured particle sizes versus *x*-velocity from the 2× FOV. As expected, the largest drops tend to be traveling the slowest due to their relatively slower acceleration by aerodynamic drag. In contrast, data from the 6× FOV is compiled by treating individual frames as independent measurements (without regard to velocity) The large, slower drops reside over a larger duration within the 6× FOV. Therefore, the large drops appear to be over counted compared to the 2× results. This is particularly evident in the volumetric size distribution in Figure 5(b).

In what follows, some simple theory is presented to correct for these biases. First simulations are used to verify accuracy when all other sources of uncertainty are removed. Following this, corrections are applied to the experimental results and shown to improve the agreement between the FOVs.

Theory

In [1] Lefebvre distinguishes between *spatial sampling* and *temporal sampling*. Spatial sampling refers to a diagnostic which measures all of the particles within a FOV at an instant in time, while temporal sampling quantifies all of the particles that pass through a fixed measurement volume over time. Here, the raw 6× DIH results, wherein every frame is processed independently, is an example of spatial sampling, while the 2× results, including particle tracking over time, is an example of temporal sampling.

Lefebvre [1] summarizes the difference between the two results and their conversion as follows:

> "If all drops in a spray travel at the same velocity, the results obtained by spatial and temporal sampling are identical. If not, the spatial drop size distribution may be converted into the temporal distribution by multiplying the number of drops of a given velocity by that velocity [1]."

This is equivalent to weighting the spatially sampled result by the inverse of the residence time of each particle within the measurement volume. Assuming the extent of the measurement volume is constant for all drop sizes, this is further equivalent to multiplying the probability of each drop size class by the mean velocity of the particles in that size class.

To illustrate the application of this theory, simulations are first considered such that all other potential sources of experimental uncertainty are removed. For clarity, a relatively simple particle field is considered. First, N particles were randomly sampled from bimodal log-normal number distributions of the form,

$$f(d) = \frac{1-\omega}{d\,\sigma_a\sqrt{2\pi}} e^{-\frac{(\ln d-\mu_a)}{2\sigma_a^2}} + \frac{\omega}{d\,\sigma_b\sqrt{2\pi}} e^{-\frac{(\ln d-\mu_b)}{2\sigma_b^2}},$$

where d is the particle diameter in micrometers, ω is the relative weight, σ is the standard deviation and μ is the mean, both on the natural log scale. The a distribution is composed of smaller particles and the b distribution is composed of larger particles.

Due to aerodynamic drag, particle velocities from the component at larger diameters are expected to be slower than the component at smaller diameters. This size-velocity correlation is imposed on the particles based on their diameter, providing *x*-velocities for each particle. Here, the functional form of the mean size-velocity correlation is chosen as

$$v_x(d) = C_1 d^{C_2} + C_3,$$

where d has units of micrometers and v_x has units of m/s. Additional variation can be incorporated with the velocity of the particle to more accurately simulate experimental measurements.

The paths for the particles are next generated by providing a random starting frame and a random starting y-height, both sampled from uniform distributions. The simulations run for a total of F_{max} frames at 20,000 fps. The resulting size and position data are then resampled in two ways. The first dataset maintains all the simulated frames but has a cut-off for a minimum particle size of $d_{min} = 50\ \mu m$, producing temporally resolved data. The second set of data maintains all the particles but down-samples the number of frames by a factor of 10, producing spatially resolved data. Both these cases show extreme versions of the experimental conditions listed in the previous section.

The temporally resolved data is then passed into a custom particle-tracking algorithm, which determines the velocity of particles by comparing two consecutive frames and matching particles with their nearest neighbor in the next frame and checking that the particle diameters are similar. The algorithm also allows for preferential velocity directions and velocity limits, which improves processing speeds and accuracy. Provided that no additional noise or quantization is introduced, the particle density is not too high and that particles do not intermittently enter and exit the field of view, the tracking efficiency is 100% and the algorithm runs in a matter of seconds. Lastly, the data are processed to create measured probability distributions for temporally resolved $f_t(d)$ and spatially resolved $f_s(d)$ data.

For simulation A, two distinct particle size distributions are simulated and no additional variation is added to the size-velocity correlation in order to better illustrate the key biases. It is important to note that a

distribution of particle sizes is necessary in order to produce a size-velocity correlation fit. Figure 7(a) shows a single frame from simulation A with $N = 5000$ and $F_{max} = 1000$. Although the weight between the two particle sizes is 50%, there appear to be more large particles in the frame because they are traveling slower.

Figure 7(b) shows the specified size-velocity correlation as well as the velocity of the tracked particles from the temporally resolved data. A fit is generated from the temporally resolved distribution that is very similar to the original size-velocity correlation. However, because the temporally resolved data only contains particles larger than d_{min}, the fit values for $\hat{v}_x(d)$ of the same form as the imposed size-velocity correlation were found to be $C_1 = -11.9$, $C_2 = 0.177$, and $C_3 = 41.1$, which are slightly different from the original correlation in Table I. The accuracy of the fit improves with increasing N and decreasing d_{min}.

The imposed underlying, measured and corrected particle number PDFs are compared in Figure 7(c). The temporally resolved data contains no particles smaller than d_{min}, which results in uniformly higher probabilities for all the particles sizes. The spatially resolved distribution, on the other hand, shows lower probabilities for smaller particles and larger probabilities for larger particles. Larger, slower drops are oversampled due to their longer residence times within the FOV. It is important to note that this would be true even if the spatially resolved results were sampled at a lower effective record rate such that no particle resides within the FOV for more than one frame, as is sometimes incorrectly suggested to remove size-velocity biases. Both distributions are clearly biased in different ways.

Table I: Conditions for Simulation A

Property	Value	Property	Value
σ_a	0.4 *ln(μm)*	ω	0.5
μ_a	3.5 *ln(μm)*	C_1	-16
σ_b	0.05 *ln(μm)*	C_2	0.15
μ_b	6.0 *ln(μm)*	C_3	46

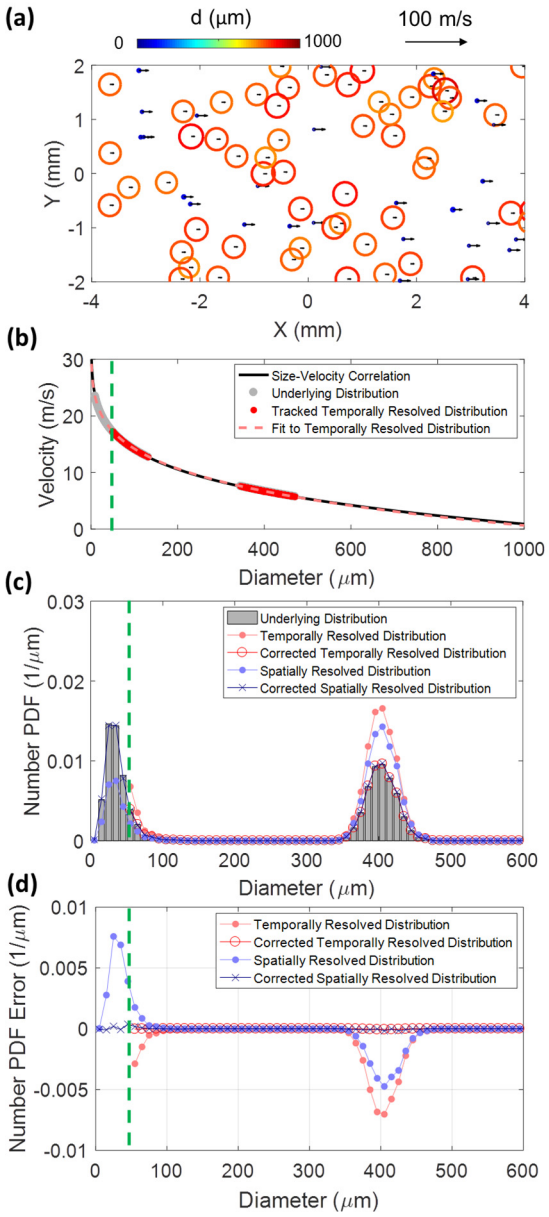

Figure 7. Simulation A results showing (a) one frame from the dataset, (b) the size-velocity distribution, (c) the particle size number PDF and (d) the error between the true underlying number PDF compared to the measured and corrected number PDFs.

The spatially resolved distribution can be used to correct for the size-velocity bias by multiplying the PDF by the velocity fit generated by the temporally resolved distribution, following the suggestion by Lefebvre [1]. Assuming that an appropriate velocity function that matches well with the underlying mean size-velocity correlation is selected and a good fit is obtained, the corrected spatially resolved PDF is,

$$f_s^*(d_i) = \frac{f_s(d_i)\hat{v}_x(d_i)}{\sum f_s(d_i)\hat{v}_x(d_i)}.$$

The resulting distribution is almost identical to the underlying distribution, as illustrated by Figure 7(d).

Next, the temporally resolved distribution is matched to the corrected spatially resolved distribution using,

$$f_t^*(d) = s_t\, f_t(d),$$

where

$$s_t = \sum_{d_i=d_{min}}^{\infty} f_s^*(d_i) \Big/ \sum_{d_i=d_{min}}^{\infty} f_t(d_i).$$

The corrected temporally resolved distribution is also similar to the underlying PDF with near-zero error for the valid size range larger than d_{min}. With no errors in tracking, the corrected PDF errors decrease with increasing N, decreasing d_{min}, and improved fitting to the true size-velocity correlation.

In many instances in the literature, the characteristic mean diameters are reported. The mean diameters are defined as,

$$D_{pq} = \left(\frac{\sum d_i^p}{\sum d_i^q}\right)^{\frac{1}{p-q}}.$$

The number population mean is defined as D_{10}, the surface area weighted mean (or Sauter mean) is defined as D_{32} and the volume weighted mean is defined as D_{43}. When these statistics are measured from spatially resolved data, corrections must also be applied such that,

$$D_{pq}^* = \left(\frac{\sum d_i^p\, \hat{v}_x(d_i)/\overline{\hat{v}_x}}{\sum d_i^q\, \hat{v}_x(d_i)/\overline{\hat{v}_x}}\right)^{\frac{1}{p-q}},$$

Where $\hat{v}_x(d_i)/\overline{\hat{v}_x}$ is the velocity estimate normalized by the average estimated velocity. This correction allows for accurate comparisons of droplet statistics.

Table II: Conditions for Simulation B

Property	Value	Property	Value
σ_a	0.4 *ln(μm)*	ω	0.2
μ_a	3.0 *ln(μm)*	C_1	-16
σ_b	0.53 *ln(μm)*	C_2	0.15
μ_b	5.0 *ln(μm)*	C_3	46

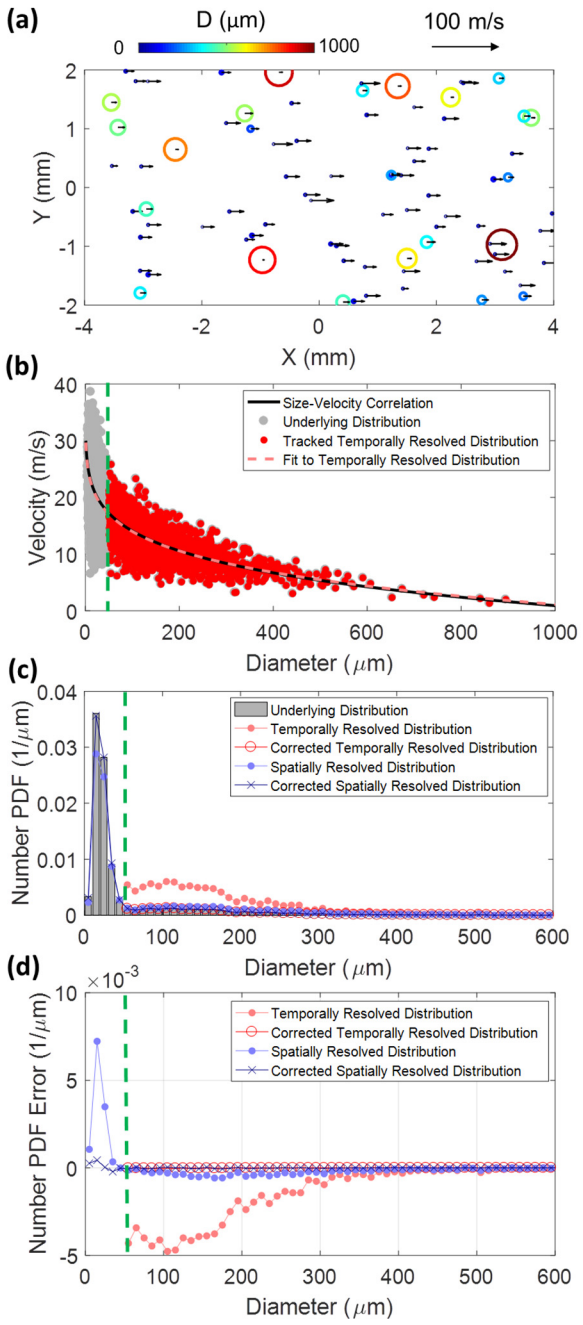

Figure 8. Simulation B results showing (a) one frame from the dataset, (b) the size-velocity distribution, (c) the particle size number PDF and (d) the error between the true underlying number PDF compared to the measured and corrected number PDFs.

A bi-modal particle size distribution and size-velocity correlation that are more similar to experimental data is demonstrated with Simulation B. The test conditions are N = 10000 and F_{max} = 1000 with additional values listed in Table I. In this simulation, there is a

larger quantity of small particles that cannot be resolved with the temporally resolved camera. An additional, normally distributed variation is added to the particle velocity such that particles with higher average velocities have more variation. A size-velocity correlation is developed using this data, as shown in Figure 8(b), and the fitted values to the temporally resolved distribution were C_1 = -16.2, C_2 = 0.147, and C_3 = 45.9, which are very similar to the input size-velocity correlation listed in Table II. This fit is used to correct the spatially resolved distribution resulting in a good match with the original underlying distribution as shown in in Figure 8(c) and (d).

Furthermore, the volume PDFs can be compared, as shown in Figure 9. Because larger particles carry more volume per particle, the temporally resolved volume PDF generally matches the underlying volume PDF well. The corrected spatially resolved distribution matches well for particles larger than d_{min} as well as particles smaller than d_{min}. These results show the validity of the proposed correction method.

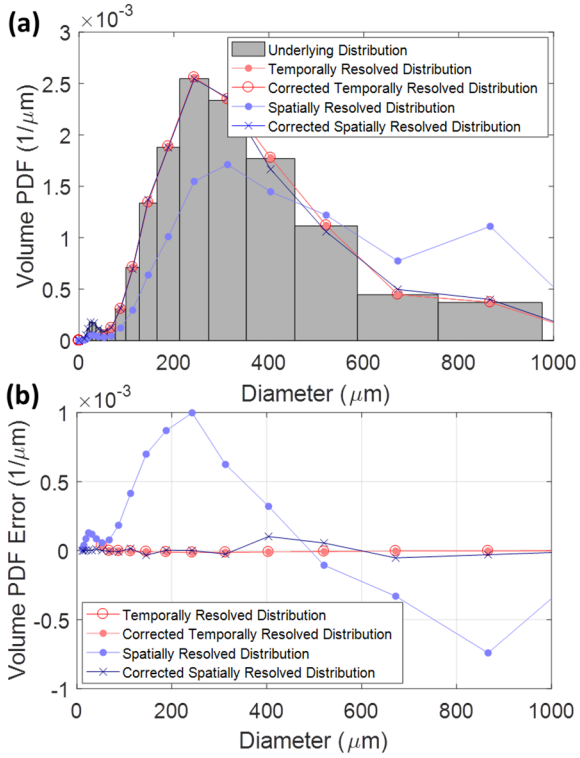

Figure 9. Simulation B results showing (a) the particle volume PDF and (d) the error between the true underlying volume PDF compared to the measured and corrected volume PDFs.

Experimental results

The previous section develops simple methods to correct size-velocity biases and validates the method via application to simulated results where all other sources of uncertainty are removed. Here, the same methods are applied to the experimental results summarized in Figure 1.

As was done in the previous section, the correlation between measured particle size and velocity is first determined from the temporally resolved (2×) FOV. The mean size-velocity relation appears to follow a power-law function, giving the best-fit curve shown in Figure 6 with fit constants C_1 = -55.9, C_2 = 0.046, and C_3 = 83.2. This relation is used to find the corrected 6× probability density shown in Figure 10(a). Finally, this is used to estimate the percentage of the total drops which fall within the limited size dynamic range of the 2× FOV, resulting in the scaled 2× probability densities.

Compared to the un-corrected PDFs in Figure 5, it is clear that the number and volume PDFs from the temporally and spatially resolved measurements match much better. The remaining differences between the two distributions from 40 to 600 μm could be attributed to the clipping of particles near the edges of the FOV. Unlike the simulation where the diameter is known, the experimental measurements may estimate a smaller particle diameter if the particle is clipped. The 6× distribution may show more clipping due to its smaller field of view, thereby measuring more smaller particles in the 40 to 200 μm range and fewer particles in the 200 to 600 μm range.

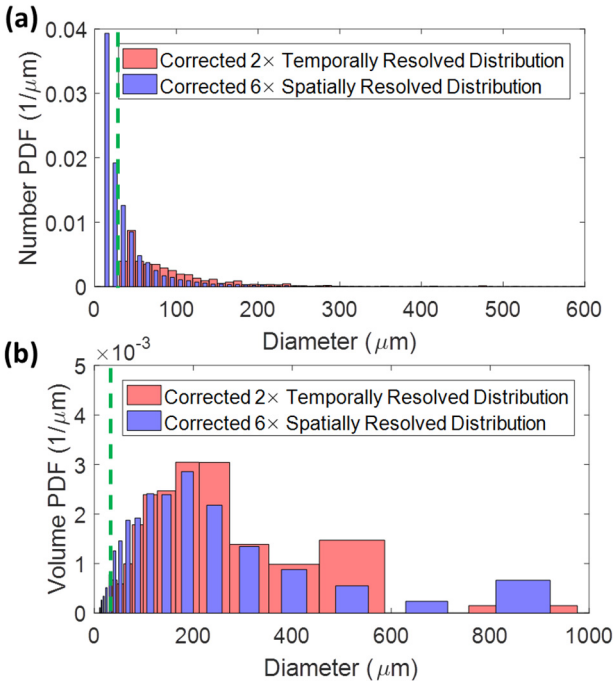

Figure 10. Application of size-velocity corrections to experimental results (a) the raw and corrected number PDFs, and (b) volume PDFs.

Table III: Characteristic Mean Diameters

Distribution	d_{min}	D_{10}	D_{32}
Measured 2×	39.3 µm	89.9 µm	195 µm
Measured 6×	12.2 µm	44.6 µm	423 µm
Corrected 6×	~0 µm	38.5 µm	278 µm

The characteristic mean diameters can also be measured and compared in Table III. The measured 2× and 6× characteristic mean diameters are very different, mostly due to the difference in the smallest diameter than can be measured d_{min}. By correcting the 6× values, which in theory creates a correction to the true underlying distribution where there is no minimum diameter (effectively $d_{min}=0$), the characteristic mean diameters from the 6× FOV decrease. The higher order mean diameter, D_{32}, begins to approach the value measured with the 2× FOV.

This experimental implementation shows how the correction method can be applied to real data. The final corrected 6× probability density represents a more accurate, high dynamic range measurement of the droplets generated by the shock-induced crossflow condition.

Conclusions

Biases due to size-velocity correlations are a common issue in many spray measurement techniques. This work specifically focuses on the distinction between temporally tracked particle measurements versus spatially collected data that has not been correlated over time.

All experimental data considered here are taken from high-speed digital in-line holography (DIH) measurements, although many of the conclusions are applicable to any image based particle measurement. In general, it is confirmed that when particles of different size classes travel at dissimilar velocities, spatially collected particle distributions are biased toward slower particles with longer effective residence times. When it is possible to measure the mean relation between particle size and particle velocity, as is done here, then these biases can be removed by weighting the distribution by the mean velocity of each size class.

When using modern high-speed cameras to perform DIH it is often necessary to trade spatial resolution (image pixel count) to achieve the desired temporal resolution. To address, this it is proposed here to combine a second simultaneous DIH measurements at lower temporal resolution but higher spatial resolution. By assuming constant particle statistics over the measurement time and extrapolating measured size-velocity correlations, it is demonstrated that size-velocity biases can be removed from the high spatial resolution (low temporal resolution) data.

Here, both fields-of-view were recorded using high-speed cameras. However, these same methods could be applied to many other image based particle measurements. For example, size-velocity correlations are easily measured using common, double-pulsed lasers and cameras (e.g. [8, 11]). If desired the proposed correction methods could be applied to convert the spatially sampled results in those works to average temporally correlated statistics. In cases where sufficient temporal and spectral resolution can be obtained, this work also shows that it is preferable to apply particle tracking to the video data in order to get accurate particle statistics, as uncorrelated snapshots contain size-velocity biases.

Acknowledgements

This work was supported by the Laboratory Directed Research and Development program at Sandia National Laboratories which is a multi-mission laboratory operated by Sandia Corporation, a Lockheed Martin Company, for the United States Department of Energy's National Nuclear Security Administration under contract No. DE-AC04-94AL85000.

References

[1] Lefebvre, A.H., *Atomization and Sprays*, Hemisphere Pub. Corp., 1989.

[2] Bachalo, W., *Atomization and Sprays*, 10(3-5): 439-474, (2000).

[3] Tropea, C., *Annual Review of Fluid Mechanics*, 43(1): 399-426, (2011).

[4] Gouesbet, G., and Gréhan, G., *International Journal of Multiphase Flow*, 72: 288-297, (2015).

[5] Xu, R., *Particuology*, 18: 11-21, (2015).

[6] Schnars, U., and Jueptner, W., *Digital holography: Digital hologram recording, numerical reconstruction, and related techniques*, Springer, 2005.

[7] Guildenbecher, D.R., Cooper, M.A., and Sojka, P.E., *Applied Optics*, 55(11): 2892-2903, (2016).

[8] Guildenbecher, D.R., Engvall, L., Gao, J., Grasser, T.W., Reu, P.L., and Chen, J., *Experiments in Fluids*, 55: 1670, (2014).

[9] Gao, J., Guildenbecher, D.R., Engvall, L., Reu, P.L., and Chen, J., *Applied Optics*, 53(27): G130-G138, (2014).

[10] Guildenbecher, D.R., Gao, J., Reu, P.L., and Chen, J., *Applied Optics*, 52(16): 3790-3801, (2013).

[11] Gao, J., Guildenbecher, D.R., Reu, P.L., Kulkarni, V., Sojka, P.E., and Chen, J., *Optics Letters*, 38(11): 1893-1895, (2013).

[12] Gao, J., Guildenbecher, D.R., Reu, P.L., and Chen, J., *Optics Express*, 21(22): 26432-26449, (2013).

[13] Chen, Y., DeMauro, E.P., Wagner, J.L., Arienti, M., Guildenbecher, D.R., Farias, P.A., Grasser, T.W., Sanderson, P.D., Albert, S.W., Turpin, A.M., Sealy, W., and Ketchum, R.S., *55th AIAA Aerospace Sciences Meeting*, 2017.

[14] Guildenbecher, D.R., Wagner, J.L., Olles, J.D., Chen, Y., DeMauro, E.P., Farias, P.A., and Grasser, T.W., *54th AIAA Aerospace Sciences Meeting*, 2016.

[15] Guildenbecher, D., *ILASS Americas 28th Annual Conference on Liquid Atomization and Spray Systems*, 2016.

[16] Katz, J., and Sheng, J., *Annual Review of Fluid Mechanics*, 42: 531-555, (2010).

[17] Meng, H., Pan, G., Pu, Y., and Woodward, S.H., *Measurement Science and Technology*, 15(4): 673, (2004).

[18] Malek, M., Allano, D., Coëtmellec, S., and Lebrun, D., *Optics Express*, 12(10): 2270-2279, (2004).